actuators

MDPI

Article

Dual Synthetic Jet Actuator and Its Applications—Part IV: Analysis of Heat Dissipation and Entropy Generation of Liquid Cooling with Dual Synthetic Jet Actuator

Ying Kang, Zhenbing Luo *, Xiong Deng, Yinxin Zhu and Zhixun Xia

College of Aerospace Science and Engineering, National University of Defense Technology, Changsha 410073, China
* Correspondence: luozhenbing@163.com

Abstract: Increasing heat flux restricts the development of the miniaturization of electronic devices. There is an urgent need for a heat dissipation method that will efficiently cool the chip. This paper presents a novel liquid cooling device based on dual synthetic jets actuator (DSJA) technology. The characteristics of the temperature and velocity field of the device are numerically studied by a three-dimensional coupled heat transfer model. The entropy generation rate caused by heat transfer and fluid friction was studied to analyze the effective work loss and irreversibility of the heat transfer process. When the DSJA is turned on, the temperature of the heat source with a heat flux of 200 W/cm^2 is 73.07 °C, and the maximum velocity is 24.32 m/s. Compared with the condition when the the DSJA is closed, the temperature decreases by 25.15 °C, and the velocity increases by nearly 20 m/s. At this time, the total inlet flow is 1.26 L/min. The larger frictional entropy generation is mainly distributed near the inlet and outlet of the channel and the jet orifice. The higher the velocity is, the more obvious the frictional entropy generation is. Due to the large temperature gradient, there is a large thermal entropy generation rate at the fluid–solid interface.

Keywords: liquid cooling; dual synthetic jets actuator; entropy generation

Citation: Kang, Y.; Luo, Z.; Deng, X.; Zhu, Y.; Xia, Z. Dual Synthetic Jet Actuator and Its Applications—Part IV: Analysis of Heat Dissipation and Entropy Generation of Liquid Cooling with Dual Synthetic Jet Actuator. *Actuators* **2022**, *11*, 382. https://doi.org/10.3390/act11120382

Academic Editor: Luigi de Luca

Received: 8 November 2022
Accepted: 16 December 2022
Published: 19 December 2022

1. Introduction

The continuous development of micro-electronic devices will depend on efficient heat dissipation technology. At present, it is a great challenge to design a heat sink with a heat flux exceeding 1 MW/m^2 [1]. Many electronic devices are damaged by overheating. When the temperature of electronic equipment increases by 10 °C, the reliability decreases by 50% [2]. Therefore, it is urgent that we seek an efficient heat dissipation technology.

Heat dissipation technology is divided into natural convection technology and forced convection technology. Forced convection technology can rapidly reduce the surface temperature of electronic devices, including spray cooling technology, microchannel cooling technology, synthetic jet technology, etc. The spray cooling device has high heat dissipation efficiency but the system is complex. The microchannel technology has the advantage of small volume and high heat transfer. Many researchers have studied the structural parameters of microchannels [3–13]. Rhombus fractal-like units [5] and spider-netted microchannels [7] have excellent heat dissipation performance. Rectangular microchannels are widely used in our lives due to their good heat dissipation and hydraulic performance. Many studies have shown that microchannels have a strong heat dissipation capability. However, to meet the heat dissipation demand, they often need to provide more pump power [14].

Synthetic jet technology [15] is an active flow control technology, which can be used in the field of heat transfer enhancement. The synthetic jet actuator (SJA) comprises a diaphragm, a cavity, and a jet orifice. The diaphragm vibrates periodically, changing the volume of the cavity. When the cavity volume is compressed, the fluid in the cavity is ejected through the jet orifice, forming a jet at the outlet of the actuator, and developing

continuously downstream. When the cavity volume is expanded, the external fluid is sucked into the cavity through both sides of the jet orifice. So far, the SJ has completed a periodic movement [15,16]. Different parameters have different effects on the heat transfer of the SJ. There is an optimal frequency to realize the maximum Nusselt number of SJs impinging on a constant heat flux disk. In addition, when the jet-to-surface distance is small, the Nusselt number increases with the jet-to-surface distance [17]. SJs can significantly destroy the thermal boundary layer to enhance heat transfer [18,19]. However, one side of the diaphragm of the SJA is located at the air side, which can easily cause ballast failure and low energy utilization.

Based on SJ technology, Luo et al. [20] invented the dual synthetic jet (DSJ) technology. The DSJ has superior performance and overcomes the problems of SJs [21]. The DSJ technology consists of two cavities, one diaphragm, and two jet outlets. The diaphragm separates the cavity. When the diaphragm vibrates, the cavity on one side expands and the cavity on the other side compresses, the jet outlet on the expanding side inhales the surrounding fluid, and the compressed side ejects the fluid in the cavity. The alternately ejected/inhaled jets interact near the outlet and merge into the DSJ, which continues to develop downstream. Research on SJ and SJA technology mostly focuses on the field of air cooling. The SJA technology has been proven to be well applied to heat dissipation in confined spaces [22].

For the heat dissipation of higher heat flux, the ability of air cooling is not enough. Therefore, some scholars have preliminarily studied the heat transfer mechanism of SJs in the liquid cooling field. Combining SJs with microchannels, the influence of the interaction between the jet and incoming flow on heat transfer is studied [23–28]. The PIV technique was used to observe the flow field of SJs underwater. Compared with the condition without SJs, the effect of an SJ makes the heat transfer increase by about 4.3 times [23]. The SJ promotes fluid mixing in the channel and enhances heat transfer [29]. It is worth noting that the SJ contributes little to the pressure drop in the channel. With a low flow rate, heat transfer can be enhanced by 130% [30]. Multiple synthetic jets can be combined with microchannels at the same time for better heat dissipation [26]. The convective heat transfer capacity of two SJs is more effective when 180° is out of phase [31,32]. The higher the frequency and amplitude of the diaphragm, the higher the convective heat transfer capacity. There is an optimal fluid inlet temperature of 297.15 K for achieving maximum heat transfer. The overall performance of the heat sink increases significantly with the Reynolds number at the inlet [32]. The underwater PIV experiment of DSJ technology shows that the jet strength is the highest when the driving frequency is 30 Hz [33]. The heat transfer characteristics and physical properties of the SJ flow field in the channel are very complex, so a comprehensive parameter study of SJAs is required [34].

Some other scholars have carried out entropy generation analysis on the studied device. Entropy generation analysis is helpful to understand the source of irreversible loss. Luis et al. [35] analyzed local entropy generation and global entropy generation of different parts of a hybrid microjet heat sink. It is found that the irreversibility of the system mainly comes from the heat transfer of the copper plate. The total entropy generation consists of thermal entropy generation and friction entropy generation. Mehdi et al. [36] found that the latter has little influence on the irreversible loss of the heat sink. Omid et al. [37] reviewed the entropy generation theory of nanofluids and introduced two calculation methods for entropy generation.

In our previous research, a side-mounted liquid cooling device was proposed [38]. Good heat transfer and flow performance are obtained. To further simplify the fluid circuit and reduce the flow resistance, this paper proposes a front-placement liquid cooling device. In this paper, the DSJ is combined with a channel for liquid cooling. The entropy generation of the cooling device is analyzed from the point of view of the second law of thermodynamics. The novelty of this study is that a new type of forwarding compound DSJ liquid cooling device is proposed. It is of great significance to solve the heat dissipation of electronic devices in a high heat flux confined space. At the same time, this study fills in

the blanks that remain from the study of DSJs by the entropy generation analysis method. The research contents of this paper are as follows: Section 2 mainly introduces the relevant models and numerical methods; Section 3 is the result discussion. The temperature field, velocity field, entropy generation, and the effect of diaphragm frequency have been studied. Section 4 is the conclusion.

2. Numerical Methods

2.1. Physical Model

In this paper, the DSJA cooling device consists of a DSJA, a channel, and an aluminum plate, as shown in Figures 1 and 2. The jet orifices are directly arranged on the upper side of the cavity to connect the channel and the actuator cavity. The channel consists of an inlet and an outlet. Jet orifices set to 5 × 5 arrays. The fluid enters the cooling device in three ways. One fluid enters the channel, and the other two fluids enter the channel through the jet orifices, through the actuator. The three converge in the channel and move downstream. The yellow arrow in Figure 1 indicates the path of fluid flow. The jet orifices are row 1, row 2, row 3, row 4, and row 5 along the positive direction of the *y*-axis.

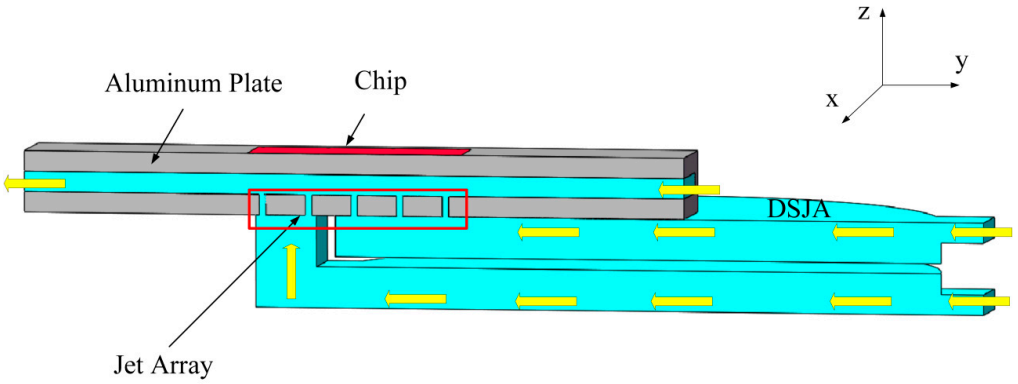

Figure 1. Schematic diagram of cooling device.

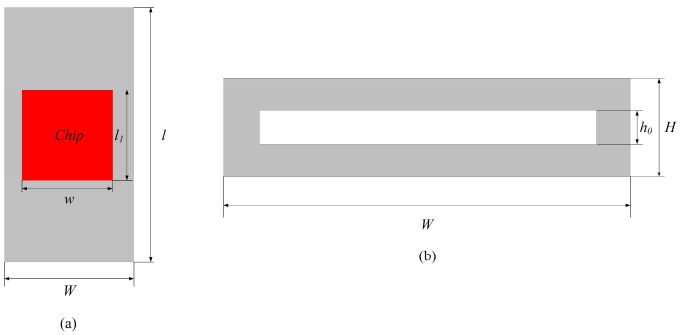

Figure 2. Schematic diagram of channel: (**a**) Vertical view; (**b**) Side view.

When the DSJA diaphragm is not vibrating, the actuator only acts as a fluid circuit. At this time, jets from the jet orifices can be regarded as steady jets. When the DSJA diaphragm vibrates upward, the cavity on the upper side of the actuator shrinks, and fluid is ejected from the third, fourth, and fifth-row jet orifices. At the same time, the cavity at the lower side of the actuator expands, and the fluid in the channel flows into the cavity at the lower side through the 1st and 2nd discharge orifices. When the DSJA diaphragm vibrates downward, the flow situation is opposite to the above process. Different jet outlets alternately eject/inhale fluid, and the formed jets fuse and develop with each other, and interacts with the incoming flow of the channel to form a violent disturbance.

2.2. Governing Equations

In this paper, a three-dimensional fluid–solid coupling model is established. The thermophysical properties of fluids and solids are considered constant. The fluid is assumed to be incompressible. The working fluid is water, and the solid is aluminum. The mass, momentum, and energy equations of the problem [25] can be written as

$$\frac{\partial \rho}{\partial t} + \nabla \cdot \rho U = 0 \tag{1}$$

$$\frac{\partial}{\partial t}(\rho U) + \nabla \cdot (\rho U U) = -\nabla p + \nabla \cdot (\overline{\tau}) \tag{2}$$

$$\frac{\partial}{\partial t}(\rho E) + \nabla \cdot (U(\rho E + p)) = \nabla \cdot \left(\lambda_{\text{eff}} \nabla \mathrm{T} + \left(\overline{\overline{\tau}}_{\text{eff}} \cdot U \right) \right) \tag{3}$$

2.3. Boundary Conditions and Numerical Solver Setting

The simulation software used in this research is Fluent. Pressure-based solver is selected for calculation. The energy equation is opened. Considering the need to solve the jet impact problem and large-scale flow changes, the SST k-ω model is selected. The calculation includes a fluid domain and a solid domain. The material of the fluid domain is water, and the material of the solid domain is aluminum.

The boundary conditions of the cooling device are set as shown in Figure 3. Considering that the cooling device is completely symmetrical, only half of the model is calculated. Symmetrical boundary conditions are adopted for the model section. The entrance of the channel and the entrance of the actuator adopt the velocity inlet boundary. The inlet velocity is 1.5 m/s and 0.3 m/s, respectively. The channel outlet is set as the pressure outlet. The chip uses a constant heat flux boundary. The inlet water temperature is 25 °C. The fluid–solid interface is set as the coupling surface. The rest are set as non-sliding walls.

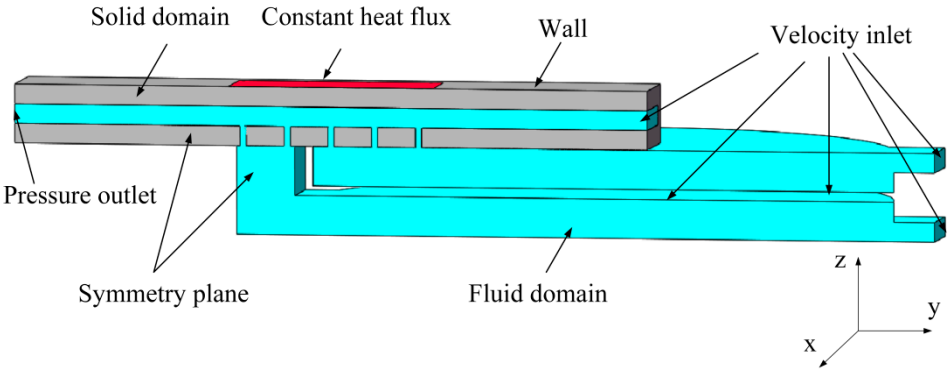

Figure 3. Boundary conditions of the calculation model.

The actuator diaphragm uses velocity inlet boundary conditions of user-defined functions (UDF) as

$$\begin{cases} u(t)_l = 0.02 \sin(2\pi f t + 0^\circ) \\ u(t)_r = 0.02 \sin(2\pi f t + 180^\circ) \end{cases} \tag{4}$$

The pressure and velocity are coupled by a SIMPLE algorithm. The relaxation factors for pressure, density, and momentum are set by default to 0.3, 1, and 0.7, respectively. The criterion of the energy equation is 10^{-6}, and the convergence criterion of mass and momentum is 10^{-3}. In this paper, the frequency is selected as f = 30 Hz [33]. The time step is set to 2.778×10^{-4} s, and the total time is 6.67 s.

2.4. Numerical Method Validation

Grid independence verification is performed on the model, as shown in Table 1. Because the model is completely symmetrical, only half of the model is used for structural

mesh generation. Three sets of grids are divided, and the $y+$ value is less than 1. The error between the number of grids (8,555,843) and the number of grids (11,713,823) is less than 8%. To ensure the calculation accuracy and velocity, 8,555,843 grids are selected for calculation, as shown in Figure 4.

Table 1. Grid independence verification.

	Grid Number	Pressure Drop (kPa)	Convergence Criteria	Base Temperature (°C)	Convergence Criteria
DSJ off	4,374,057	4.35	0.685%	97.82	1.082%
	8,555,843	4.38	0.000%	98.22	0.677%
	11,713,823	4.38	-	98.89	-
DSJ on(T)	4,374,057	5.93	18.767%	76.31	0.883%
	8,555,843	6.78	7.123%	76.61	0.493%
	11,713,823	7.30	-	76.99	-

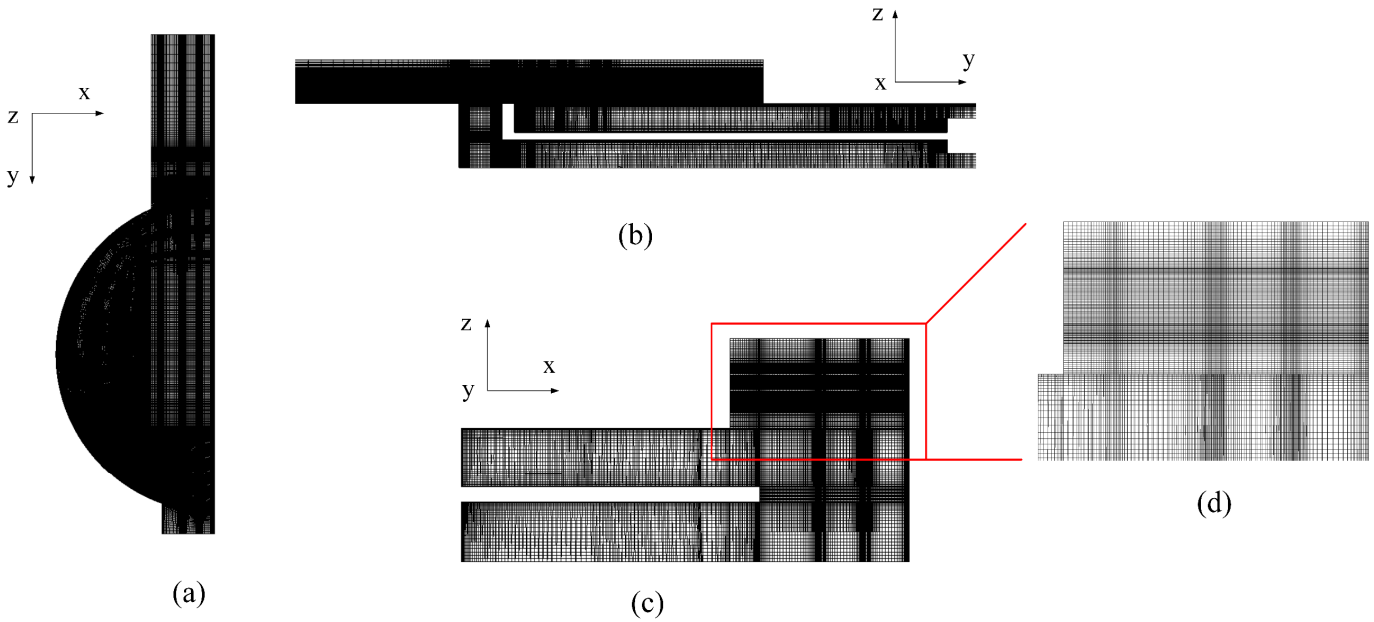

Figure 4. Structural grid of the model: (**a**) Vertical view; (**b**) Front view; (**c**) Side view; (**d**) Local details of (**c**).

The experimental model in reference [33] is selected to verify the numerical method in this paper. As shown in Figure 5, the RNG k-ε model and SST k-ω model are selected. The velocity distribution at 2 mm away from the DSJ orifice was studied. The results show that the SST k-ω model is in better agreement with the experiment.

2.5. Relevant Definitions

The hydraulic diameter of the channel is

$$D_h = \frac{2w\ h_0}{w + h_0} \tag{5}$$

where w, and h_0 are the channel width and height, respectively. In this paper, D_h = 1.8182 mm.

The channel Reynolds number Re_c [28] and the DSJ Reynolds number Re_{dsj} are defined as follows:

$$Re_c = \frac{\rho u_{in} D_h}{\mu} \tag{6}$$

$$Re_{dsj} = \frac{\rho u_{dsj} d}{\mu} \tag{7}$$

where u_{in} = 1.5 m/s, u_{dsj} = 24.32 m/s, and d = 0.36 mm are the flow velocity of the channel inlet, the maximum flow velocity at the exit of the actuator, and the diameter of the jet

orifice, respectively. The value of the channel Reynolds number is 2714. The range of jet Reynolds numbers Re_{dsj} is 43,998.192.

The Nusselt number of a channel is defined as

$$Nu = \frac{D_h h}{\lambda} \tag{8}$$

where $h = \frac{q}{(T_w - T_f)}$ is the convective heat transfer coefficient of DSJA, where T_w and T_f are the solid surface temperature and the fluid temperature, respectively.

The volume entropy production rate includes the entropy production rate caused by irreversible heat transfer and the irreversible flow loss caused by fluid friction. All formulas [36] are as follows:

$$\dot{S}'''_{gen,total} = \dot{S}'''_{gen,thermal} + \dot{S}'''_{gen,frictional} \tag{9}$$

$$\dot{S}'''_{gen,thermal} = \frac{\lambda_f}{T_f^2}\left[\left(\frac{\partial T}{\partial x}\right)^2 + \left(\frac{\partial T}{\partial y}\right)^2 + \left(\frac{\partial T}{\partial z}\right)^2\right] \tag{10}$$

$$\dot{S}'''_{gen,frictional} = \frac{\mu}{T_f}\left\{2\left[\left(\frac{\partial u}{\partial x}\right)^2 + \left(\frac{\partial v}{\partial y}\right)^2 + \left(\frac{\partial w}{\partial z}\right)^2\right] + \left(\frac{\partial u}{\partial y} + \frac{\partial v}{\partial x}\right)^2 + \left(\frac{\partial u}{\partial z} + \frac{\partial w}{\partial x}\right)^2 + \left(\frac{\partial v}{\partial z} + \frac{\partial w}{\partial y}\right)^2\right\} \tag{11}$$

u, v, w are velocity components in x, y, z directions respectively.

The total entropy generation is the integral sum of thermal entropy generation and frictional entropy generation in the entire cooling device.

$$\int\int\int_\Omega \dot{S}_{gen} dV = \int\int\int_\Omega \dot{S}_{gen,thermal} dV + \int\int\int_\Omega \dot{S}_{gen,frictional} dV \tag{12}$$

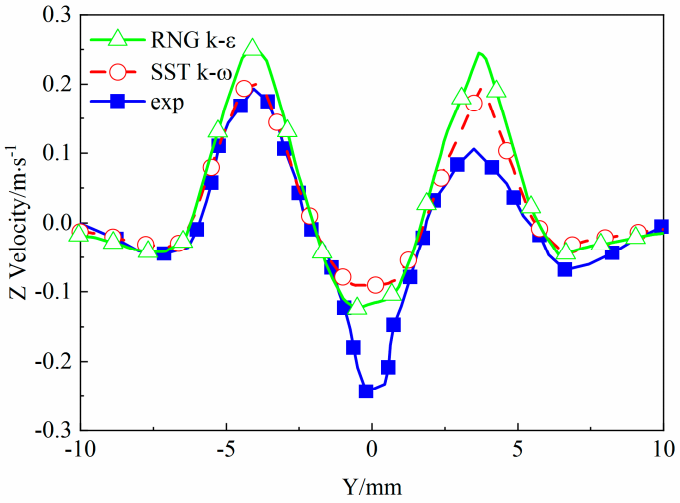

Figure 5. Numerical simulation and experimental [33] verification of DSJ underwater (z = 2 mm).

3. Results

3.1. Temperature Field

To study the enhanced heat transfer mechanism of the DSJ, the central section of the channel (section x = 28.5 mm) is taken as an example for analysis. The inlet velocity of the channel is 1.5 m/s, and the inlet velocity of DSJA is 0.3 m/s. The heat flux of the heat source is 200 W/cm^2. The heat source is located at -5.25 mm $< y <$ 5.25 mm.

The temperature field of the channel is shown in Figure 6. The average temperature of the chip is 120.35 °C. It is observed that the substrate temperature near the outlet is higher than that of the inlet. This is because the fluid takes away heat along the flow direction,

increasing the fluid temperature. A thermal boundary layer attached to the substrate is gradually thickening along the flow direction, weakening the heat transfer capability. There are partitions between adjacent channels to enhance the heat conduction effect.

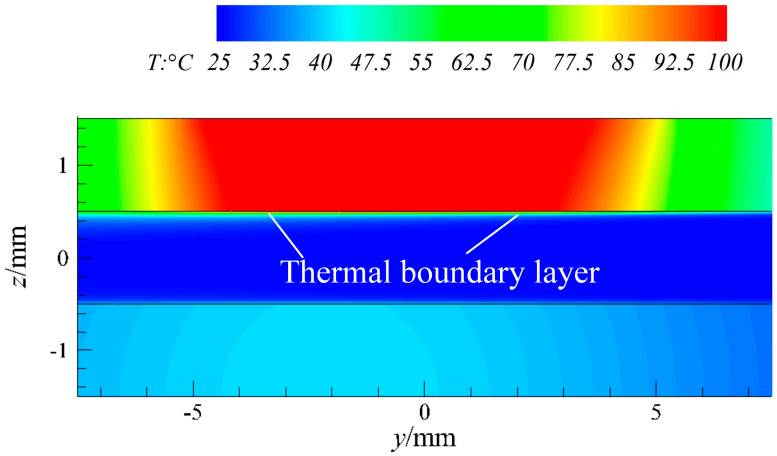

Figure 6. Temperature distribution of channel's center section (x = 28.5 mm).

The temperature fields of the DSJ when off and the DSJ when on are shown in Figures 7 and 8, respectively. In Figure 7, the maximum temperature of the heat source is 98.22 °C. The thermal boundary layer gradually develops and thickens along the channel's top wall from the channel inlet. It is destroyed in the jet impact area. Compared with other areas, a part of the thermal boundary layer is observed above the fourth and fifth row of jet orifices, considering the jet deflection caused by the weak jet of the upper cavity itself and the incoming flow. The impact damage ability to the thermal boundary layer is weakened. The existence of the thermal boundary layer will deteriorate the heat transfer, which will help to reduce the temperature of the actuator.

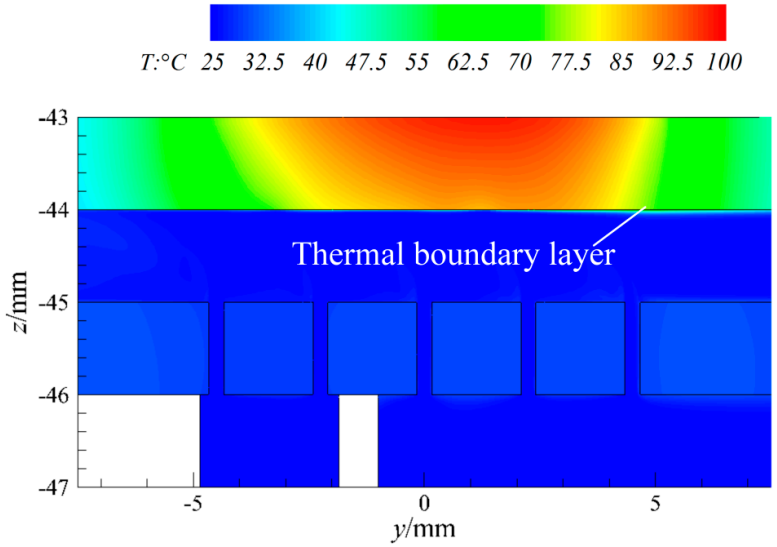

Figure 7. Temperature distribution (DSJ off) of channel's center section (x = 28.5 mm).

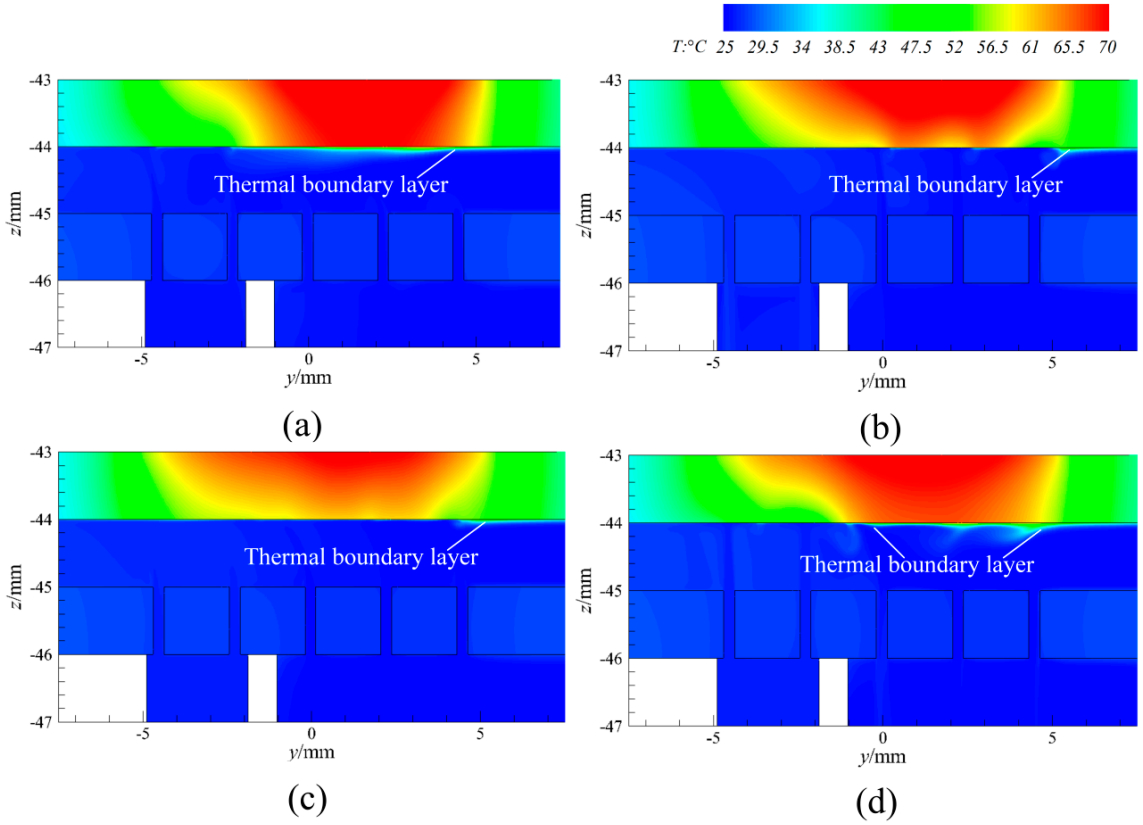

Figure 8. Temperature distribution of channel's center section (x = 28.5 mm) (DSJ on): (**a**) 0 T (1 T); (**b**) 0.25 T; (**c**) 0. 5 T; (**d**) 0.75 T.

Compared with the DSJ when off, the maximum temperature drop of the heat source is 25.15 °C when the DSJ is on, as shown in Figure 8. The alternating vibration of the diaphragm of the DSJA has a periodic effect on the temperature distribution of the aluminum plate. At 0 T (1 T), the thermal boundary layer was observed above the third, fourth, and fifth-row jet orifice. Consider that the upper cavity is in the suction stage at this time. The attachment of the thermal boundary layer results in an obvious high-temperature region. The temperature of the aluminum plate above the first and second rows of jet orifices is obviously lower, which is caused by jet impingement cooling. At 0.25 T, the temperature contour shows an obvious low-temperature area, and the thermal boundary layer has been destroyed. At this time, the upper cavity is in the ejection stage, and the jet ability is strong. At 0.5 T, the temperature distribution near the impact surface is relatively uniform. Consider the weakening stage of the jet from the upper cavity. At 0.75 T, the temperature of the corresponding impact area of the first and second row of jet orifices decreased significantly. This is due to the impact of the jet at the outlet of the lower cavity. Influenced by the flow of the jets and incoming flow in the suction channel of the cavity, a partially disordered thermal boundary layer was observed. Then, the cooling device enters the stage of 0 T (1 T) again, and the above process is repeated. The periodic vibration of the diaphragm brings about the periodic change of the temperature of the aluminum plate, and the reciprocating disturbance of the jet and its interaction with the incoming flow strengthen the convection heat transfer.

The distribution of Nu on the impact surface (z = 44 mm) along the y direction is shown in Figure 9. When the DSJ is off, the distribution of Nu is low in the middle and high on both sides. This is because the middle area is close to the heat source and has a higher temperature. Both sides have low-temperature regions because they are far away from heat sources and close to the inlet and outlet of the channel. When the DSJ is on, the distribution of Nu varies at different times. The distribution of Nu is opposite

to the temperature distribution of the DSJA in Figure 8. The area where the thermal boundary layer is damaged has a large Nu number. The importance of breaking the thermal boundary layer for enhancing heat transfer is further illustrated. In addition, at the moment of 0.75 T~0 T (1 T), a larger Nu number is observed in the area of $y < 0$. It indicates that the lower cavity is in the injection stage at this time. Since there are only two rows of jet outlets in the lower cavity, the jet velocity is higher. At 0.75 T, the impact area is wider, corresponding to the wider Nu distribution in Figure 9. In a word, the effect of the DSJ increases the Nu number and presents a "wavy" Nu distribution curve. It reflects the effective disturbance of the DSJ to the flow field.

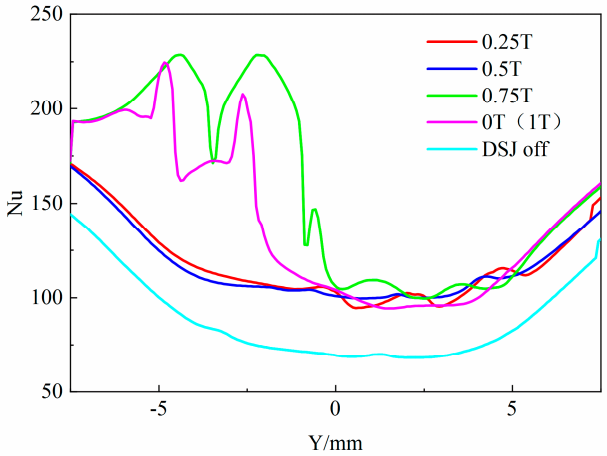

Figure 9. The distribution of *Nu* on the impact surface (z = 44 mm) along the y direction.

3.2. Flow Field Characteristics

This section studies the flow field characteristics of cooling devices, as shown in Figures 10–13. It can be observed from Figure 10 that when there is only a channel, the streamlines in the channel are parallel to each other along the streamlines. The fluid in the channel does not affect each other. Thick velocity boundary layers were observed near the upper and lower walls of the channel.

When the DSJ is off, the maximum velocity in the flow field reaches 4.5 m/s. The fluid entering the channel flows parallel to the channel at the beginning, and its flow path is disturbed when it passes near the jet orifice under the influence of the jet. The fluid becomes disordered. The channel flow is "squeezed" upward by the jet, and a low-velocity area (the blue part in Figure 11) is observed between adjacent jets. At the same time, the jet deflects along the flow direction under the action of channel flow. The fourth and fifth rows of jets deflect most obviously. It is consistent with the phenomenon described in Section 3.1.

When the DSJ is on, the flow field distribution of one cycle of the DSJA is shown in Figures 12 and 13. At 0 T, the actuator diaphragm vibrates downward. The upper cavity volume expands while the lower cavity volume compresses. An obvious vortex structure was observed in the upper cavity. Since the vibration of the diaphragm is small at this time, the flow from the actuator will inhibit the suction of fluid in the channel. In addition, when the jet interacts with the incoming flow, the flow in the channel is disordered, while when the jet is far away, the flow in the channel remains stable. The region of a steady fluid flow corresponds to the gradually thickened thermal boundary layer in Figure 8a. It further shows that the enhancement of fluid kinetic energy destroys the thermal boundary layer and enhances heat transfer. At 0.25 T, the upper cavity ejects fluid, and the jet impinges on the aluminum plate surface to form an obvious low-temperature area. At 0.5 T, the diaphragm is in a balanced position. The ability of the upper cavity to eject the jet is weakened. The jet deflects under the influence of incoming flow. At 0.75 T, the lower cavity ejects a strong jet. An obvious vortex structure is formed in the channel, and the temperature of the jet impingement zone is obviously reduced. At the same time, it was observed that the fluid in some channels was sucked into the upper cavity. The large

vortex structure was observed above the third, fourth, and fifth jet orifices, because it was affected by the three actions of ejected fluid, inhaled fluid, and incoming flow. The resulting temperature distribution is consistent with that observed in Figure 8.

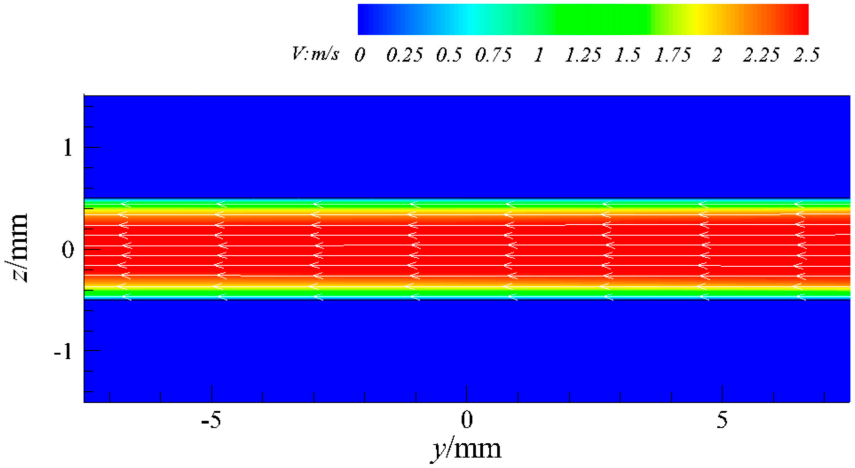

Figure 10. Velocity distribution of channel's center section (x = 28.5 mm).

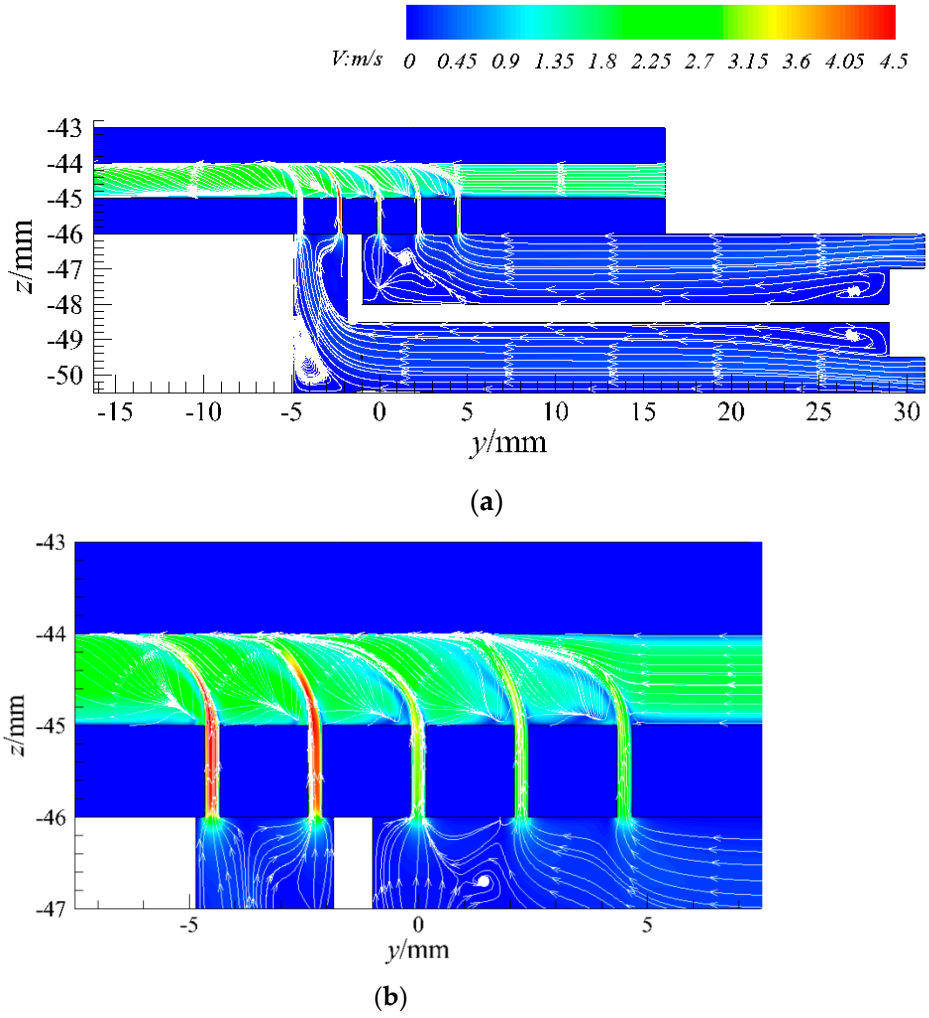

Figure 11. Velocity distribution (DSJ off) of channel's center section (x = 28.5 mm): (**a**) overall view; (**b**) partial enlarged view of jet orifice area.

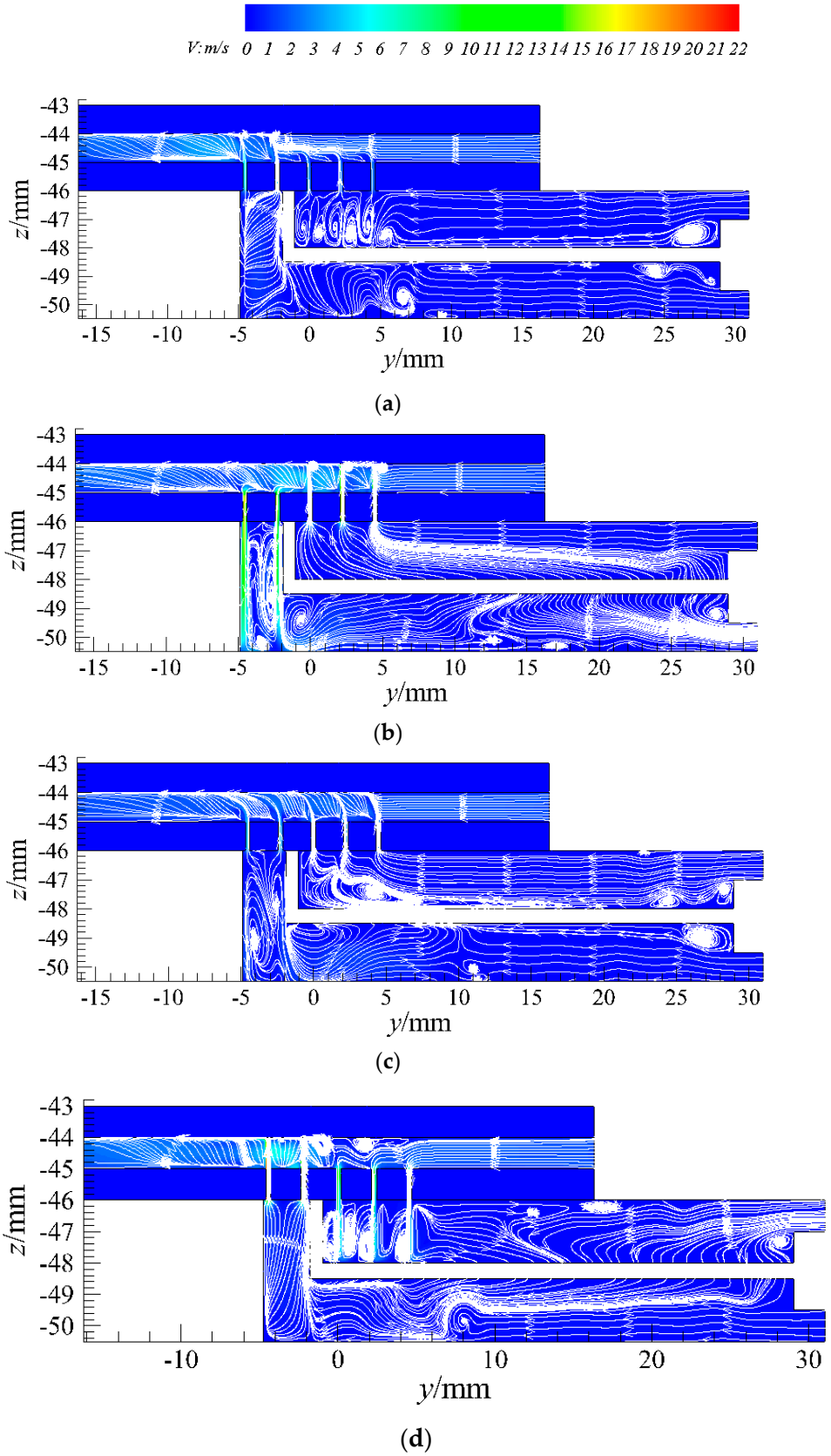

Figure 12. Velocity distribution of channel's center section (x = 28.5 mm, overall view) (DSJ on): (**a**) 0 T (1 T); (**b**) 0.25 T; (**c**) 0.5 T; (**d**) 0.75 T.

To further analyze the flow field characteristics of the DSJA, the vorticity distribution of the DSJA is shown in Figure 14. When the DSJ is off, only large vortices are observed in the channel, especially near the jet orifices, as shown in Figure 14a. The vorticity distribution of one cycle after the DSJ is turned on is shown in Figure 14b–e. It can be found that the vorticity increases significantly, and the vorticity distribution also changes significantly. Under the action of the DSJ, the fluid in the channel is affected by alternate blowing and suction, forming a periodic disturbance. A larger range of large vorticity distribution was observed in the channel. In addition, the reciprocating up and down the vibration of the diaphragm increases the vorticity in the cavity. It further shows that the fluid mixing under the action of the DSJ is enhanced, which enhances the convective heat transfer capability of the fluid.

3.3. Entropy Generation Analysis

The entropy generation rate is used to reflect the irreversibility of the heat transfer and flow process. This section studies the entropy generation characteristics of the DSJA from the perspective of the second law of thermodynamics. The total entropy production rate includes the entropy production rate caused by irreversible heat transfer and the irreversible flow loss caused by fluid friction.

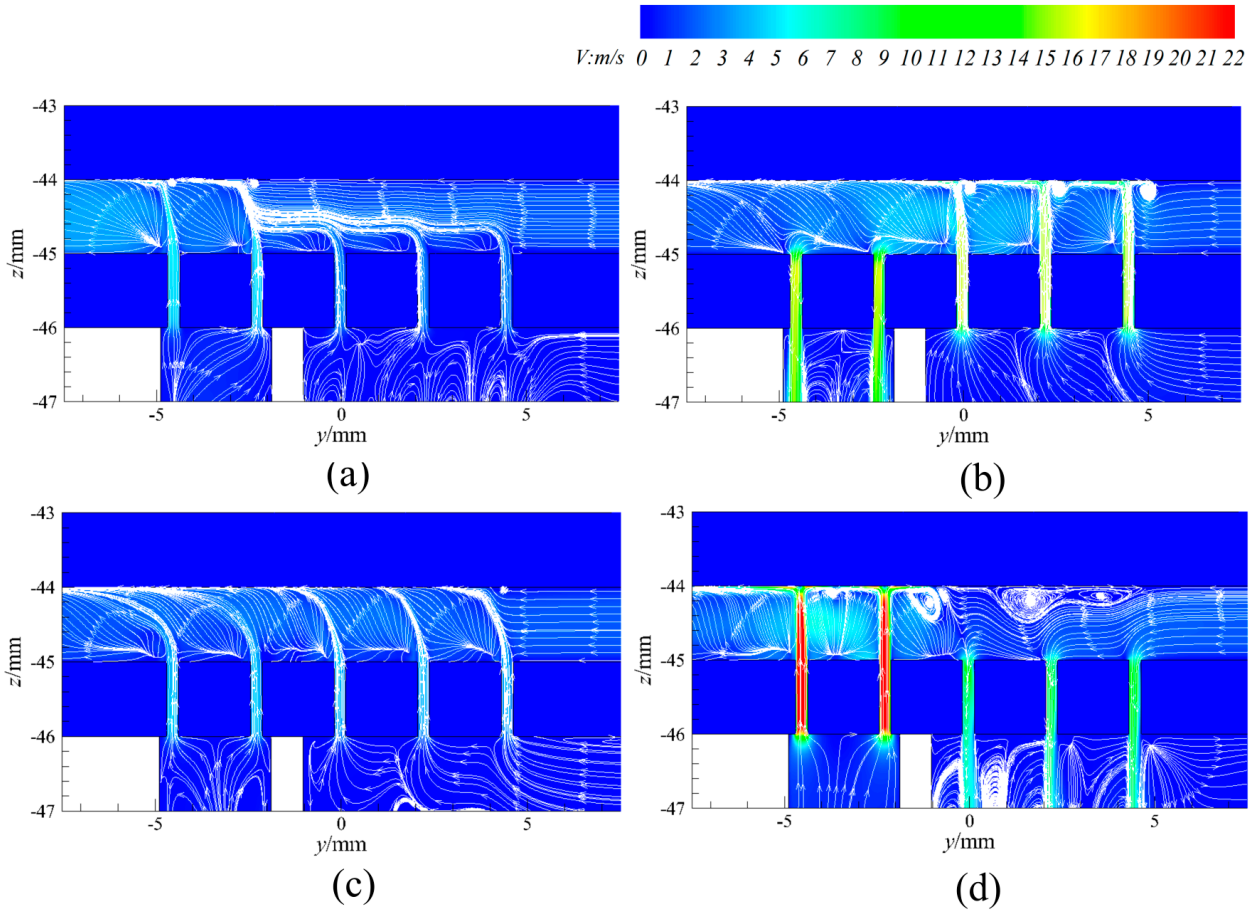

Figure 13. Velocity distribution of channel's center section (x = 28.5 mm, partial enlarged view of jet orifice area) (DSJ on): (**a**) 0 T (1 T); (**b**) 0.25 T; (**c**) 0.5 T; (**d**) 0.75 T.

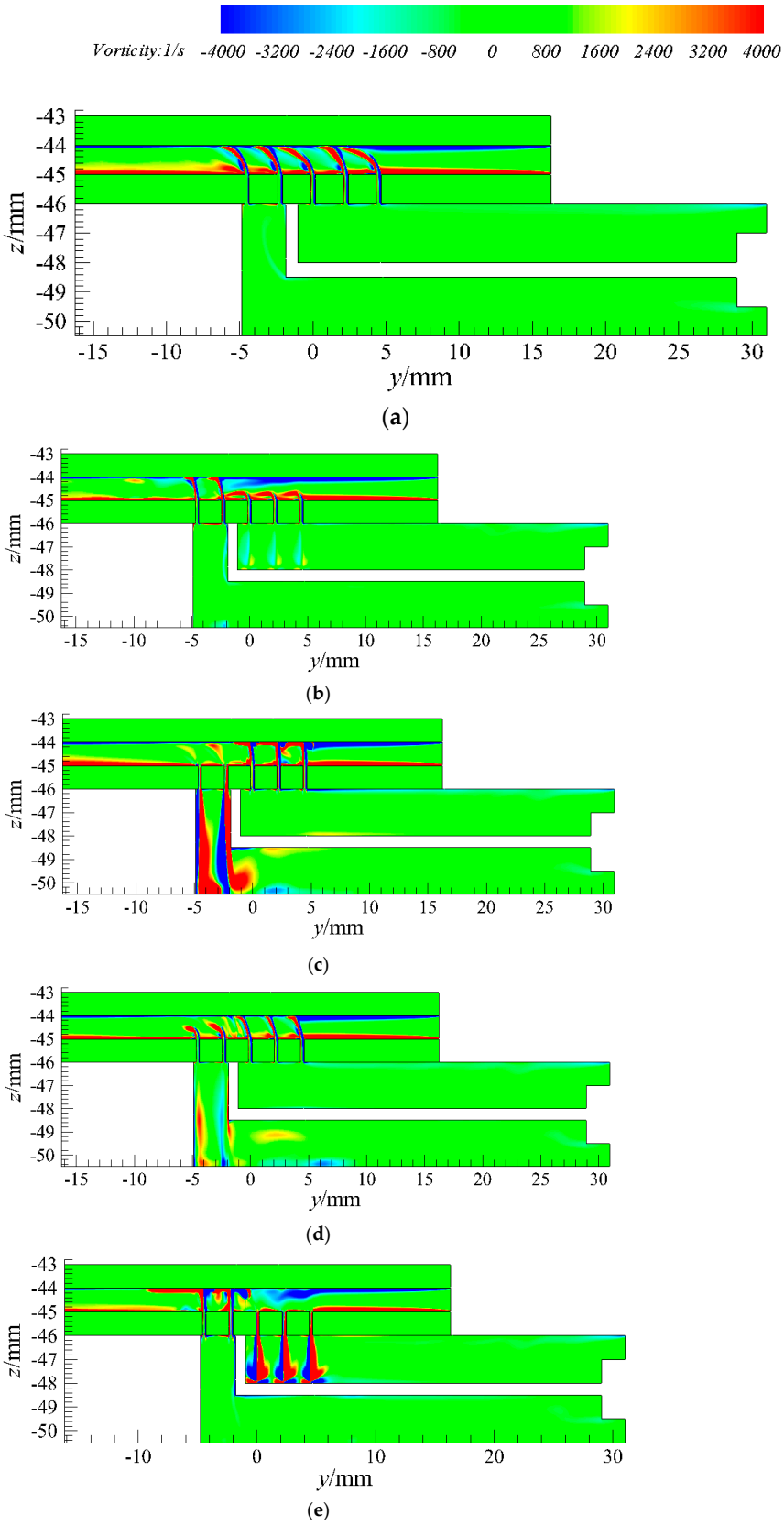

Figure 14. X vorticity distribution of channel's center section (x = 28.5 mm, overall view): (**a**) DSJ off; (**b**) 0 T (1 T); (**c**) 0.25 T; (**d**) 0.5 T; (**e**) 0.75 T (**d**,**e**, DSJ on).

The thermal entropy generation rate of the DSJ when off and the DSJ when on are shown in Figures 15 and 16. When the DSJ is off, the higher thermal entropy generation rate is mainly located at the interface between the fluid domain and the solid domain. This is mainly due to the large temperature gradient in these places. The water temperature at the inlet and outlet of the channel is low, the temperature gradient is large, and the thermal entropy generation rate is higher. When the DSJ is on, a high thermal entropy generation rate is also observed at the fluid–solid interface. The heat transfer in the region where the thermal boundary layer exists is poor and the thermal entropy generation rate is high. Under the disturbance of the DSJ, the distribution of the thermal entropy generation rate near the jet orifice is obviously disordered. At the same time, the impingement of the jet makes the thermal boundary layer thinner and the thermal entropy generation rate lower.

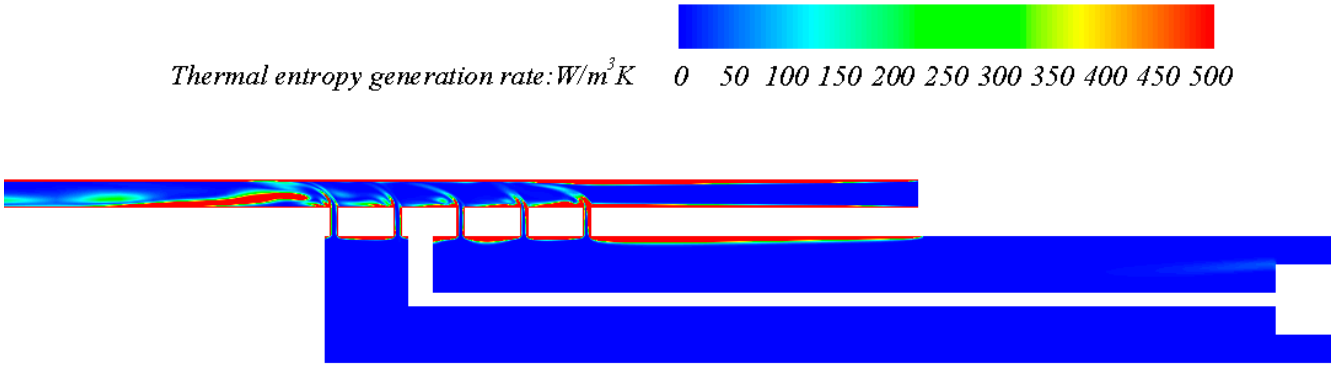

Figure 15. Thermal entropy generation rate in the fluid domain (x = 28.5 mm, DSJ off).

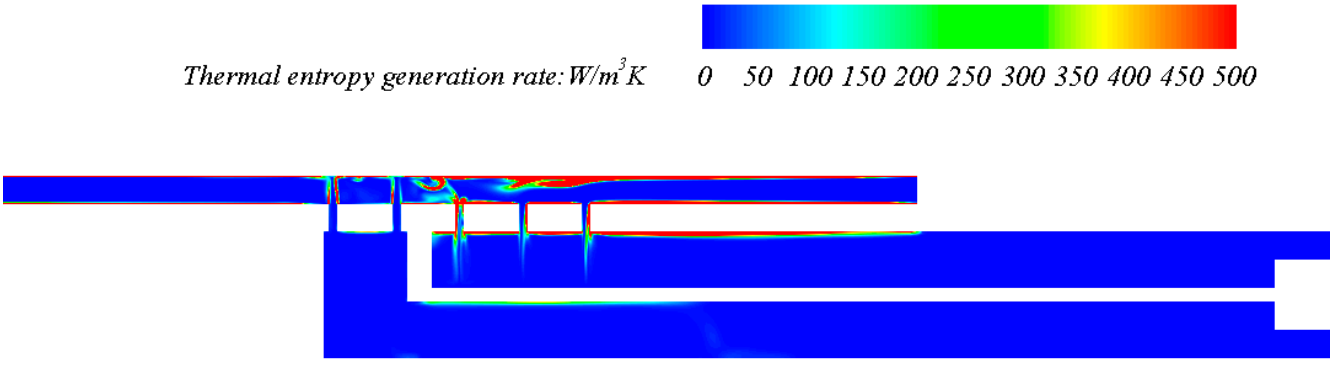

Figure 16. Thermal entropy generation rate in the fluid domain (x = 28.5 mm, 0.75 T of DSJ on).

The frictional entropy generation rate of the DSJ when off and the DSJ when on are shown in Figures 17 and 18. The higher frictional entropy generation rate is mainly located near the inlet and outlet of the channel and the jet orifice, especially in the jet impingement area. This is mainly due to the large velocity gradient at the inlet and outlet of the channel. The jet orifice diameter is small, and the velocity will change suddenly. When the DSJ is off, the jet deflects under the influence of incoming flow. The deflection area has a low-velocity area. Therefore, the frictional entropy generation rate is large. This is consistent with the phenomenon observed in Figure 11.

When the DSJ is on, Figure 18 observed the frictional entropy output value in a larger area than when the DSJ is off. This is because the diaphragm is at a limited position of downward vibration at this moment. The lower cavity ejects the jet and the upper cavity inhales the jet. The high strength of the jet results in a large velocity gradient. Observing the DSJ-off and DSJ-on cases, it can be found that the frictional entropy generation increases with the increase of the velocity of the DSJA. This is due to the increase in velocity gradient and the decrease in temperature. In the whole heat dissipation device, the greater the

velocity, the more obvious the frictional entropy generation. Small channels and jet orifices favor greater velocity gradients.

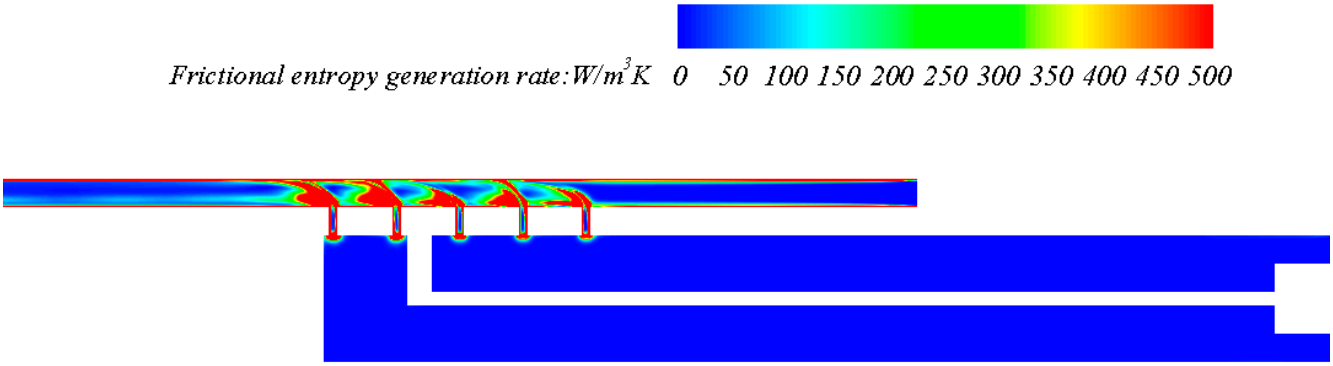

Figure 17. Frictional entropy generation rate in the fluid domain (x = 28.5 mm, DSJ off).

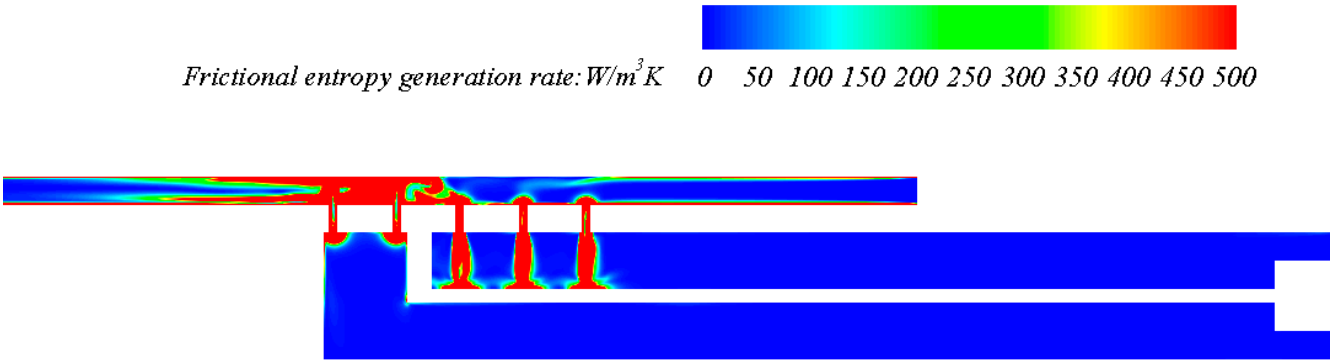

Figure 18. Frictional entropy generation rate in the fluid domain (x = 28.5 mm, 0.75 T of DSJ on).

The total entropy generation rate of the DSJ when off and the DSJ when on are shown in Figures 19 and 20. It can be seen that the high total entropy generation rate is mainly located near the jet orifice and the inlet and outlet of the channel. We use Formula (12) to calculate the overall value of entropy, as shown in Table 2. It can be seen that the total entropy generation is dominated by the value of thermal entropy generation because the contribution of frictional entropy generation is very small. Since there is no velocity in the solid domain, its frictional entropy generation rate is 0. The total entropy generation in the fluid domain is much greater than that in the solid domain. Moreover, the total entropy generation of the DSJ when off is 0.01309, while the value of the DSJ when on is only 0.00414. The entropy production is reduced, and the latter is more than three times lower than the former. It indicates that the irreversible loss of the DSJA is greatly reduced.

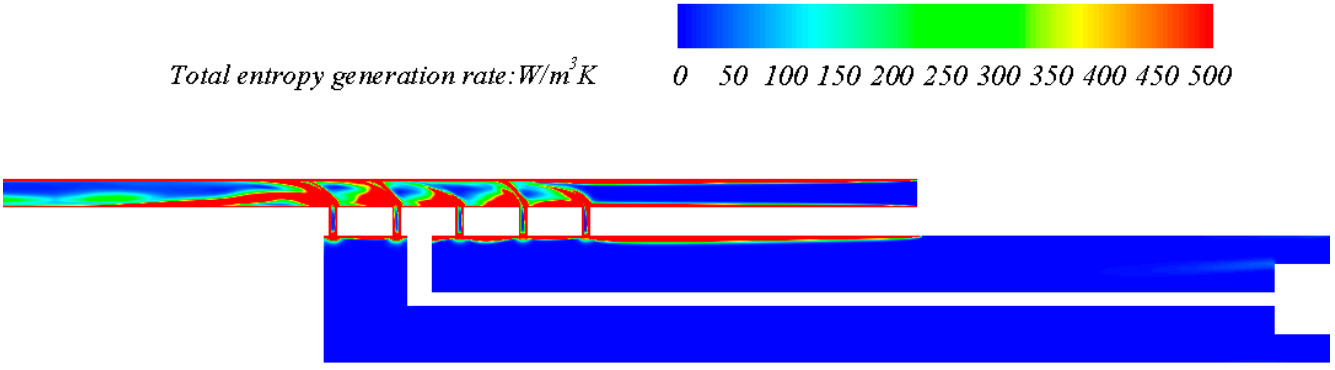

Figure 19. Total entropy generation rate in the fluid domain (x = 28.5 mm, DSJ off).

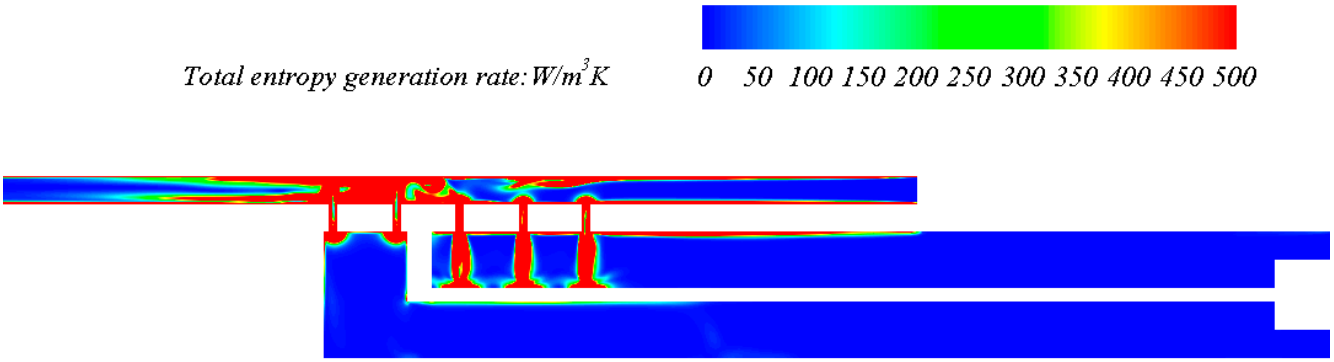

Figure 20. Total entropy generation rate in the fluid domain (x = 28.5 mm, 0.75 T of DSJ on).

Table 2. Thermal entropy generation, frictional entropy generation, and total entropy generation in different areas of the cooling device.

Case	Fluid			Solid		Cooling Device		
	Thermal	Frictional	Total	Thermal	Total	Thermal	Frictional	Total
DSJ off	0.01298	0.00005	0.01303	0.00006	0.00006	0.01304	0.00005	0.01309
DSJ on (0.75 T)	0.00380	0.00030	0.00410	0.00004	0.00004	0.00384	0.00030	0.00414

3.4. Effect of Diaphragm Frequency

The influence of the diaphragm frequency on the performance of the cooling device was studied, keeping other settings unchanged.

The change of the periodic average temperature of the wall along the y direction along the channel with the diaphragm frequency is shown in Figure 21. The temperature distribution of the impact surface is not monotonic with the frequency. The impact surface temperature is the highest when the frequency is 10 Hz. When the frequency is 30 Hz, the impact surface has the lowest temperature and the temperature change is more obvious. The temperature near the jet impingement point is lower than that in other areas. This is because the effect of the dual synthetic jets strengthens the fluid-mixing and improves the convection heat transfer capacity of the fluid.

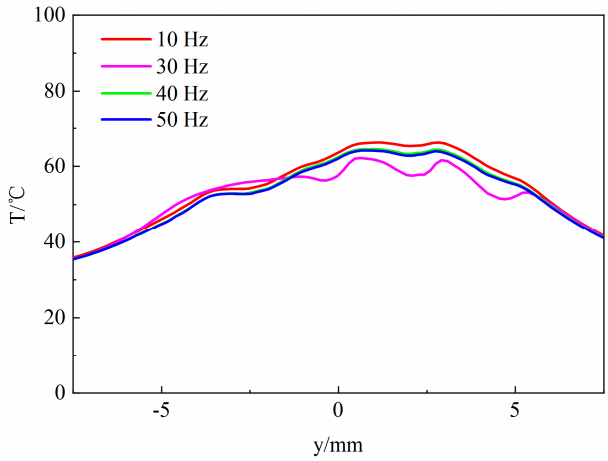

Figure 21. The change of the periodic average temperature of the wall along the y direction along the channel with the diaphragm frequency (x = 28.5 mm).

The channel inlet and outlet pressure drop changes with the diaphragm frequency as shown in Figure 22. The channel inlet and outlet pressure drop is the lowest when the diaphragm frequency is 10 Hz and the highest when the diaphragm frequency is 40 Hz.

It shows that the pressure drop at the inlet and outlet of the channel is not monotonous with the change in the diaphragm frequency. It can be seen from Figures 21 and 22 that the cooling device has the best performance due to the optimal frequency. In the frequency range studied in this paper, the best comprehensive performance of the heat sink is obtained when the frequency is 30 Hz.

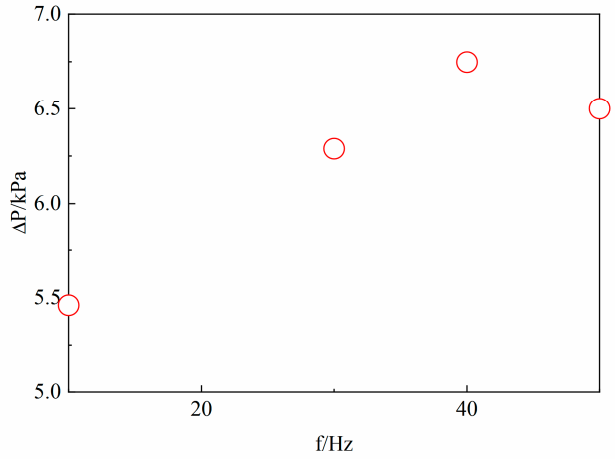

Figure 22. The channel inlet and outlet pressure drop changes with the diaphragm frequency (x = 28.5 mm).

4. Conclusions

In this paper, combined with the DSJ technology, a forward liquid cooling device is designed. The heat transfer and flow characteristics of the device are analyzed. The entropy generation of the DSJA is analyzed from the point of view of the second law of thermodynamics. The main conclusions are as follows

- When the DSJ is off, the cooling device observes an asymmetric temperature distribution. The maximum temperature reaches 98.22 °C. When the DSJ is on, the maximum temperature is only 73.07 °C. A 25.60% heat transfer enhancement was achieved. The temperature field of the cooling device changes periodically with the DSJ. The thermal boundary layer attached to the impact surface was periodically destroyed by the DSJ. It is helpful to enhance convection heat transfer.
- When the DSJ is off, the jet deflects under the influence of a flow velocity of 1.5 m/s in the channel. It is difficult to achieve full-impact heat dissipation on the wall. The DSJ on solves this problem. At this time, the DSJ can directly impact the wall and interacts with the incoming flow to enhance mixing. The rich vortex structure is helpful for convection heat transfer.
- The results of entropy generation analysis show that total entropy generation mainly comprises the contribution of thermal entropy generation, and the influence of frictional entropy generation is small. The entropy generation of the DSJ when on is much lower than that of the DSJ when off.
- The optimal frequency results in the best overall performance of the cooling device. This section studies the performance of the cooling device when the diaphragm frequency is 10 Hz, 30 Hz, 40 Hz, and 50 Hz. It is found that the device has the best comprehensive performance when the frequency is 30 Hz.

Author Contributions: Writing: original draft, Y.K.; Writing: review and editing, Z.L., X.D., Y.Z. and Z.X. All authors have read and agreed to the published version of the manuscript.

Funding: This research was funded by the National Natural Science Foundation of China, grant numbers 11872374, 11972369; the Science and Technology Innovation Program of Hunan Province, grant number 2021RC3075; and the Natural Science Foundation of Hunan Province of China, grant number 2021JJ40672.

Institutional Review Board Statement: Not applicable.

Informed Consent Statement: Not applicable.

Data Availability Statement: Not applicable.

Conflicts of Interest: The authors declare no conflict of interest.

References

1. Hao, X.H.; Peng, B.; Xie, G.N.; Chen, Y. Efficient on-chip hotspot removal combined solution of thermoelectric cooler and mini-channel heat sink. *Appl. Therm. Eng.* **2016**, *100*, 170–178. [CrossRef]
2. Viswanath, R.; Wakharkar, V.; Watwe, A.; Lebonheur, V. Thermal performance challenges from silicon to systems. *Int. Technol. J.* **2000**, *3*, 1–16.
3. Tuckerman, D.B.; Pease, R.F.W. High-performance heat sinking for VLSI. *IEEE Electron Device Lett.* **1981**, *2*, 126–129. [CrossRef]
4. Zeng, S.; Lee, P.S. Topology optimization of liquid-cooled microchannel heat sinks: An experimental and numerical study. *Int. J. Heat Mass Transf.* **2019**, *142*, 118401. [CrossRef]
5. Zhuang, D.W.; Yang, Y.F.; Ding, G.L.; Du, X.Y.; Hu, Z.T. Optimization of microchannel heat sink with rhombus fractal-like units for electronic chip cooling. *Int. J. Refrig.* **2020**, *116*, 108–118. [CrossRef]
6. Alugoju, U.K.; Dubey, S.K.; Javed, A. Optimization of converging and diverging microchannel heat sink for electronic chip cooling, IEEE Transactions on Com-ponents. *Packag. Manuf. Technol.* **2020**, *10*, 817–827. [CrossRef]
7. Tan, H.; Wu, L.W.; Wang, M.Y.; Yang, Z.H.; Du, P.A. Heat transfer improvement in microchannel heat sink by topology design and optimization for high heat flux chip cooling. *Int. J. Heat Mass Transf.* **2019**, *129*, 681–689. [CrossRef]
8. Wang, R.; Qian, J.Y.; Wei, T.; Huang, H.J. Integrated closed cooling system for high-power chips. *Case Stud. Therm. Eng.* **2021**, *26*, 100954. [CrossRef]
9. Ma, D.D.; Xia, G.D.; Wang, J.; Yang, Y.C.; Jia, Y.T.; Zong, L.X. An experimental study on hydrothermal performance of microchannel heat sinks with 4-ports and offset zigzag channels. *Energy Convers. Manag.* **2017**, *152*, 157–165. [CrossRef]
10. Zhang, J.R.; Zhang, T.T.; Prakash, S.; Jaluria, Y. Experimental and numerical study of transient electronic chip cooling by liquid flow in microchannel heat sinks. *Numer. Heat Transf. Part A Appl.* **2014**, *65*, 627–643. [CrossRef]
11. Xie, G.N.; Liu, J.; Zhang, W.H.; Sunden, B. Analysis of flow and thermal performance of a water-cooled transversal wavy microchannel heat sink for chip cooling. *J. Electron. Packag.* **2012**, *134*, 041010. [CrossRef]
12. Tseng, P.H.; Tsai, K.T.; Chen, A.L.; Wang, C.C. Performance of novel liquid-cooled porous heat sink via 3-D laser additive manufacturing. *Int. J. Heat Mass Transf.* **2019**, *137*, 558–564. [CrossRef]
13. Chiu, H.C.; Jang, J.H.; Yeh, H.W.; Wu, M.S. The heat transfer characteristics of liquid cooling heatsink containing microchannels. *Int. J. Heat Mass Transf.* **2011**, *54*, 34–42. [CrossRef]
14. Robinson, A.J. A thermal–hydraulic comparison of liquid microchannel and impinging liquid jet array heat sinks for high-power electronics cooling. *IEEE Trans. Compon. Packag. Technol.* **2009**, *32*, 347–357. [CrossRef]
15. Smith, B.L.; Glezer, A. The formation and evolution of synthetic jets. *Phys. Fluids* **1998**, *10*, 2281–2297. [CrossRef]
16. van Buren, T.; Whalen, E.; Amitay, M. Vortex formation of a finite-span synthetic jet: Effect of rectangular orifice geometry. *J. Fluid Mech.* **2014**, *745*, 180–207. [CrossRef]
17. Bazdidi-Tehrani, F.; Eghbali, A.; Karami, M. Influence of jet-to-surface distance and frequency on unsteady heat transfer and mass flowrates in an impingement synthetic jet. *J. Enhanc. Heat Transf.* **2013**, *20*, 115–136. [CrossRef]
18. Zhang, J.Z.; Tan, X.M. Experimental study on flow and heat transfer characteristics of synthetic jet driven by piezoelectric actuator. *Sci. China Ser. E Technol. Sci.* **2007**, *50*, 221–229. [CrossRef]
19. Jagannatha, D.; Narayanaswamy, R.; Chandratilleke, T.T. Analysis of a synthetic jet-based electronic cooling module. *Numer. Heat Transf. Part A Appl.* **2009**, *56*, 211–229. [CrossRef]
20. Luo, Z.B.; Xia, Z.X.; Liu, B. New Generation of Synthetic Jet Actuators. *AIAA J.* **2006**, *44*, 2418–2419. [CrossRef]
21. Luo, Z.B.; Zhao, Z.J.; Deng, X.; Wang, L.; Xia, Z.X. Dual Synthetic Jets Actuator and Its Applications—Part I: PIV Measurements and Comparison to Synthetic Jet Actuator. *Actuators* **2022**, *11*, 205. [CrossRef]
22. Deng, X.; Luo, Z.B.; Xia, Z.X.; Gong, W.J. Experimental investigation on the flow regime and impingement heat transfer of dual synthetic jet. *Int. J. Therm. Sci.* **2019**, *145*, 105864. [CrossRef]
23. Jagannatha, D.; Chandratilleke, T.T.; Narayanaswamy, R. Interactive flow behaviour and heat transfer enhancement in a microchannel with cross flow synthetic jet. *Int. J. Emerg. Multidiscip. Fluid Sci.* **2010**, *2*, 27–43. [CrossRef]
24. Lee, A.; Yeoh, G.H.; Timchenko, V.; Reizes, J. Numerical computation and investigation of the characteristics of microscale synthetic jets. *Model. Simul. Eng.* **2011**, *2011*, 12. [CrossRef]
25. Pokharel, P. Convective Heat Transfer Enhancement of a Channel-Flow Using Synthetic Jet. Doctoral Dissertation, The University of Mississippi, Oxford, MS, USA, May 2021.
26. Lee, A.; Yeoh, G.H.; Timchenko, V.; Reizes, J.A. Heat transfer enhancement in micro-channel with multiple synthetic jets. *Appl. Therm. Eng.* **2012**, *48*, 275–288. [CrossRef]
27. Lau, G.E.; Mohammadpour, J.; Lee, A. Cooling performance of an impinging synthetic jet in a microchannel with nanofluids: An Eulerian approach. *Appl. Therm. Eng.* **2021**, *188*, 116624. [CrossRef]

28. Qiu, Y.L.; Hu, W.J.; Wu, C.J.; Chen, W.F. Flow and heat transfer characteristics in a microchannel with a circular synthetic jet. *Int. J. Therm. Sci.* **2021**, *164*, 106911. [CrossRef]
29. Giachetti, B.; Fénot, M.; Couton, D.; Plourde, F. Influence of Reynolds number synthetic jet dynamic in crossflow configuration on heat transfer enhancement. *Int. J. Heat Mass Transf.* **2018**, *118*, 1–13. [CrossRef]
30. Fang, R.X.; Khan, J.A. Active heat transfer enhancement in single-phase microchannels by using synthetic jets. *J. Therm. Sci. Eng. Appl.* **2013**, *5*, 011006. [CrossRef]
31. Mohammadpour, J.; Salehi, F.; Lee, A.; Brandt, L. Nanofluid heat transfer in a microchannel heat sink with multiple synthetic jets and protrusions. *Int. J. Therm. Sci.* **2022**, *179*, 107642. [CrossRef]
32. Mohammadpour, J.; Salehi, F.; Lee, A. Performance of nano encapsulated phase change material slurry heat transfer in a microchannel heat sink with dual-circular synthetic jets. *Int. J. Heat Mass Transf.* **2022**, *184*, 122265. [CrossRef]
33. Peng, L.; Luo, Z.B.; Deng, X.; Yang, S.K. Experimental investigation on characteristics of flow field and propulsion of dual synthetic jets in water. *Acta Aerodyn. Sin.* **2017**, *35*, 290–298.
34. Ikhlaq, M.; Yasir, M.; Demiroğlu, M.; Arik, M. Synthetic Jet Cooling Technology for Electronics Thermal Management—A Critical Review. IEEE Transactions on Components. *Packag. Manuf. Technol.* **2021**, *11*, 1156–1170. [CrossRef]
35. Paniagua-Guerra, L.E.; Ramos-Alvarado, B. Efficient hybrid microjet liquid cooled heat sinks made of photopolymer resin: Thermo-fluid characteristics and entropy generation analysis. *Int. J. Heat Mass Transf.* **2020**, *146*, 118844. [CrossRef]
36. Bahiraei, M.; Heshmatian, S.; Keshavarzi, M. A decision-making based method to optimize energy efficiency of ecofriendly nanofluid flow inside a new heat sink enhanced with flow distributor. *Powder Technol.* **2019**, *342*, 85–98. [CrossRef]
37. Mahian, O.; Kianifar, A.; Kleinstreuer, C.; Al-Nimr, M.A.; Pop, I.; Ahmet, Z.; Wongwises, S.S. A review of entropy generation in nanofluid flow. *Int. J. Heat Mass Transf.* **2013**, *65*, 514–532. [CrossRef]
38. Kang, Y.; Luo, Z.B.; Deng, X.; Cheng, P.; Peng, C.; He, W.; Xia, Z.X. Numerical study of a liquid cooling device based on dual synthetic jets actuator. *Appl. Therm. Eng.* **2023**, *219*, 119691. [CrossRef]